

Energy Advances

Accepted Manuscript

This article can be cited before page numbers have been issued, to do this please use: R. Arya, T. Dagar, A. Thomas, M. N. Singh, A. K. Sinha and H. Arora, *Energy Adv.*, 2026, DOI: 10.1039/D6YA00006A.



This is an Accepted Manuscript, which has been through the Royal Society of Chemistry peer review process and has been accepted for publication.

Accepted Manuscripts are published online shortly after acceptance, before technical editing, formatting and proof reading. Using this free service, authors can make their results available to the community, in citable form, before we publish the edited article. We will replace this Accepted Manuscript with the edited and formatted Advance Article as soon as it is available.

You can find more information about Accepted Manuscripts in the [Information for Authors](#).

Please note that technical editing may introduce minor changes to the text and/or graphics, which may alter content. The journal's standard [Terms & Conditions](#) and the [Ethical guidelines](#) still apply. In no event shall the Royal Society of Chemistry be held responsible for any errors or omissions in this Accepted Manuscript or any consequences arising from the use of any information it contains.

1 Role of pH in Tailoring Ni-Co Hydroxide Nanostructures for Energy 2 Storage Applications

3 Rajkamal Arya^{a*}, Tanya Dagar^b, Arpit Thomas^{c,d}, M.N. Singh^e, A. K. Sinha^{a*}, Harpreet Singh
4 Arora^{c*}

5 ^{a*}Department of Physics, School of Advanced Engineering, UPES, Dehradun, Uttarakhand-
6 248007, India

7 ^bDepartment of Chemistry, School of Advanced Engineering, UPES, Dehradun, Uttarakhand-
8 248007, India

9 ^cDepartment of Mechanical Engineering, Shiv Nadar Institution of Eminence, deemed to be
10 University, India (UP)- 201310

11 ^dCentre for Inter-Disciplinary Research and Innovation, University of Petroleum and Energy
12 Studies, Bidholi Via-Prem Nagar, Dehradun-248007

13 ^eAccelerator Physics and Synchrotron Utilization Division, Raja Ramanna Centre for
14 Advanced Technology, Indore 452013, India

15
16 **Abstract:** Nano-sized bimetallic Nickel-Cobalt hydroxide [NiCo(OH)₄] with a 1:1 Co/Ni
17 atomic ratio was synthesized via a surfactant-free co-precipitation-hydrothermal method,
18 where the solution pH was systematically varied to direct structural evolution. The growth
19 process begins with the nucleation of hydroxide nanoplates, followed by dissolution and
20 recrystallization into stacked, hexagonal, disc-like architectures. Among the prepared samples,
21 the material synthesised at pH 9.0 exhibited the most favourable electrochemical behaviour,
22 delivering a high specific capacitance of 621 F g⁻¹ at 0.5 A g⁻¹ and retaining 400 F g⁻¹ at 10 A
23 g⁻¹, surpassing samples obtained at pH 8.0, 10.0, and 11.5. Morphological, structural, and
24 spectroscopic characterisations confirmed that the enhanced performance of NCH-2 arises
25 from its porous nanostructure, defect centres, and improved ion/electron transport kinetics for
26 energy storage applications.



27 Keywords: Co-precipitation/hydrothermal synthesis, pH value, surface morphology, Defect
28 sites.

29 1. Introduction:

30 Energy demand has increased rapidly in recent years. The need for alternative and green energy
31 sources arises from the depletion of fossil fuel reserves and the resulting carbon emissions from
32 their use ^{1,2}. To address these issues and keep up with the always-rising need for energy,
33 renewable energy sources, including wind, solar, and hydroelectricity, should be encouraged.
34 Due to the intermittent nature of these renewable resources, efficient energy storage systems
35 must be improved. Among various energy storage systems, electrochemical energy storage is
36 most widely used due to its high efficiency, long cycle life, and design versatility. It mainly
37 includes secondary ion batteries and supercapacitors, the latter comprising electric double-
38 layer capacitors (EDLCs) and pseudo-capacitors (PCs). EDLCs store charge through ion
39 adsorption at the electrode-electrolyte interface, offering excellent cycling stability but low
40 capacitance ($\sim 100 \text{ F g}^{-1}$). PCs, in contrast, involve fast surface redox reactions, yielding 10-50
41 times higher capacitance but limited stability. Carbon-based materials are commonly employed
42 for EDLCs, while transition metal oxides such as RuO_2 and IrO_2 serve as high-capacitance PC
43 electrodes despite cost constraints. Therefore, the first-row transition metal layered hydroxides,
44 particularly Co and Ni hydroxides, have been the subject of many studies ^{3,4}. Better specific
45 capacitance and rate capacity have been reported for hydroxides compared to oxides ⁵. Our
46 group has reported significant oxygen vacancies in $\alpha\text{-FeCo}_2(\text{OH})_6$, which may act as functional
47 centres for charge storage ⁶. In addition to the defect, crystallinity and crystal structure (space
48 group-P-3m1) ⁷, morphology consisting of surface area to volume ratio ⁸, average pore size and
49 size distribution ⁹, accessibility of redox-active sites, and mass transport channels ¹⁰ affect the
50 electrochemical performance of an electrode material. It has been reported that these
51 parameters can be tuned by varying the synthesis parameters during hydrothermal synthesis of



52 electrode materials. Among the synthesis parameters, reaction temperature, hydrothermal time,
53 pH of the solution, and reaction chemistry can be varied to achieve suitable material parameters
54 for the best electrochemical properties^{11–13}. Transition metal hydroxides such as NiCo(OH)₄
55 (NCH) crystallise in α , β , and γ phases, where the β -phase (P $\bar{3}m1$) is stable, the α -phase is
56 metastable, and the γ -phase is unstable. The α -phase, with a larger interlayer spacing (~ 7 Å),
57 facilitates ion intercalation/deintercalation, enhancing capacitance. During cycling, $\alpha \rightarrow \beta$
58 transformation occurs, while overcharging may reverse it. Co(OH)₂ exhibits a high theoretical
59 capacitance (~ 3600 F g⁻¹). In bimetallic hydroxides, synergistic interactions between metal ions
60 enhance electrical conductivity, ion diffusion, and active site density. For example,
61 FeCo₂(OH)₆ with oxygen vacancies on Co sites shows improved redox activity, demonstrating
62 that bimetallic synergy significantly boosts electrochemical performance.

63 It is well reported in the literature that α -TM hydroxide samples exhibit better initial energy
64 density but demonstrate poorer cyclic stability and rate capability than β -TM hydroxides. [Yin
65 et al.¹⁴, Akhtar et al.¹⁵ Rajkamal et al.¹⁶]. Yi et al.¹⁷ have reported that α/β phase synergies
66 lead to improved electrochemical performance. Optimized α/β mixed-phase samples show
67 enhanced capacity and superior capacity retention (~ 108 % after 1000 cycles at a current
68 density of 20 mA cm⁻²) compared to ~ 50 % in the α -phase and ~ 87 % in the β -phase. The
69 improved performance is attributed to the more stable structure and better electrical
70 conductivity of the β -phase, along with the higher interlayer spacing in the α -phase, which
71 facilitates efficient ion intercalation and charge transport. These combined effects are likely
72 responsible for the superior electrochemical performance observed in the α/β mixed-phase
73 sample in this study. Akhtar et. al. has synthesised nanoflowers of Ni(OH)₂ and have achieved
74 high capacitance of 1511 F g⁻¹ at a current density of 10 mA cm⁻² and 100 % capacity retention
75 after 5000 cycles at 50 mA cm⁻². The cyclic stability is higher for the mixed phase than both α
76 and β pure phases. These studies propose a synergy between better phase stability of β phase



77 and higher initial capacitance of α phase; which in optimised ratio results in good initial
78 capacitance and higher cyclic as well as rate efficiencies, as observed in this study.

79 In current study, NiCo(OH)₄ (NCH) samples prepared under systematically varied pH
80 conditions demonstrated marked differences in specific capacitance, highlighting the crucial
81 role of synthetic control in achieving high-performance electrode materials. This approach
82 underscores the importance of defect engineering and tailored nanostructure in advancing
83 bimetallic hydroxide-based energy storage technologies. The pH of the reaction medium during
84 synthesis plays a crucial role in influencing the morphology, defect concentration, structural
85 stability, and electrical conductivity of the resulting materials. These factors directly affect the
86 electrochemical performance, including specific capacitance, cyclic stability, and rate
87 capability.

88 Recent studies have highlighted that optimizing the pH conditions can significantly enhance
89 electrochemical properties. For instance, Bhatt et al.¹⁸ reported that controlled pH conditions
90 lead to improved specific capacitance ($\sim 3061 \text{ F g}^{-1}$ at 0.5 A g^{-1}), excellent cyclic stability (\sim
91 99% retention after 5000 cycles), and superior rate capability in Ni-Co-based hydroxide
92 systems. Similarly, Wang et al.¹⁹ demonstrated that pH tuning influences the preferential
93 growth direction and morphology of Ni-Co-Mn hydroxide nanostructures, which in turn
94 enhances electrochemical performance. These studies clearly indicate that careful control of
95 synthesis parameters such as pH is essential for optimizing electrochemical behavior. Hu et al.
96²⁰ synthesized layered double Ni-Co hydroxide nanosheets by optimizing the pH conditions.
97 The optimized material exhibited excellent electrochemical performance, delivering a high
98 energy density of $\sim 48.57 \text{ Wh kg}^{-1}$ at a power density of 800 W kg^{-1} , along with nearly 100%
99 capacity retention after 10,000 cycles at a current density of 10 A g^{-1} . Xiang-Yu You et al.²¹
100 reported the synthesis of transition metal hydroxides using a metal tetrafluoroborate precursor.
101 In their study, the pH of the reaction medium was carefully controlled by varying the



102 concentration of 2-methylimidazole, which effectively induced precipitation and influenced
103 the structural evolution of the material. These studies further emphasize that controlled pH
104 conditions during synthesis play a crucial role in tailoring morphology, structural properties,
105 and ultimately enhancing electrochemical performance.

106 We establish a correlation between pH-dependent structural features and electrochemical
107 performance. By combining structural characterization with detailed kinetic analysis using
108 Dunn's model, the study reveals how an optimized balance between diffusion-controlled and
109 capacitive contributions governs the superior performance of the NCH (pH-09) sample. This
110 work provides deeper insight into the role of pH in tuning ion transport, defect states, and
111 charge storage mechanisms, which is not extensively addressed in previous reports.

112 NCHs nanostructures with varying proportions of α and β phases were synthesised
113 hydrothermally using ammonia hydroxide to adjust solution pH to 8.0, 9.0, 10.0, and 11.5,
114 resulting in samples labelled NCH-1, NCH-2, NCH-3 and NCH-4 respectively. The sample
115 formed at pH 9.0 (NCH-2) displayed the most favourable electrochemical properties, achieving
116 a specific capacitance of 1230 F g^{-1} at 5 mV s^{-1} , which was significantly higher than the other
117 samples. Galvanostatic charge-discharge (GCD) measurements further confirmed its superior
118 rate capability, delivering 622 F g^{-1} at 0.5 A g^{-1} and 400 F g^{-1} at 10 A g^{-1} . Detailed
119 characterisation demonstrated that its enhanced performance is due to a higher density of
120 structural disorder/defect sites such as cobalt vacancies and oxygen interstitials, which
121 facilitate efficient charge storage and ideal ion diffusion. The enhanced electrochemical
122 kinetics of the NCH series are consistent with recent advancements in defect engineering for
123 transition metal hydroxides. Recent reports by Gao et al.²² highlight that the introduction of
124 structural defects effectively tunes the electronic structure and enhances carrier concentration,
125 thereby providing additional extrinsic pseudo capacitance. Furthermore, Bhatt et al.²³ have
126 identified that oxygen vacancies and lattice distortions in nickel-cobalt nanostructures act as



127 catalytic centres that lower charge transfer resistance and optimize ion adsorption.
128 Consequently, the structural disorder inferred from our XRD and electrochemical data suggests
129 a high density of active sites, facilitating the superior rate performance of the NCH-2 electrode.
130 A comparison of the electrochemical performance of the sample NCH-2 with other bimetallic
131 hydroxide and oxide materials without complex compositional modifications reported in the
132 literature is shown in Table S1.

133 2. Experiments section:

134 2.1. Materials:

135 Cobalt (II) nitrate hexahydrate ($\text{Co}(\text{NO}_3)_2 \cdot 6\text{H}_2\text{O}$) and Nickel nitrate hexahydrate
136 ($\text{Ni}(\text{NO}_3)_2 \cdot 6\text{H}_2\text{O}$) were procured from LOBA CHEMIE PVT.LTD. India. Ammonium
137 hydroxide (NH_4OH , 25% NH_3) and Potassium hydroxide (KOH) were obtained from Sigma-
138 Aldrich (Lyon, France), and Emplura/Merck life science PVT.LTD. respectively. Chemical
139 reagents are analytical grades and were used as received without further purification. Double
140 distilled water was used throughout the experiments.

141 2.2 Synthesis process:

142 A Co-precipitation/hydrothermal method was used to synthesized Nano-sized bimetallic
143 $\text{NiCo}(\text{OH})_4$ (NCH) using ammonia hydroxide (NH_4OH , 25%) to adjust solution pH to 8.0, 9.0,
144 10.0, and 11.5, resulting in samples labelled NCH-1, NCH-2, NCH-3 and NCH-4 respectively.
145 A standard process involved dissolving 1.48 g of (Nickel and cobalt (1:1)) nitrate hexahydrate
146 in 60 mL of Deionised (DI) water. Add respective amount of NH_4OH dropwise in above
147 solution and to ensure complete mixing, the solution was then magnetically stirred for 1 hour.
148 The resultant suspension was put into a stainless-steel autoclave lined with Teflon and heated
149 for 4 hours at 120°C . To get the final powder samples, the precipitate was collected after



150 naturally cooling to room temperature, extensively cleaned many times with ethanol and DI
151 water to get rid of any remaining ions and contaminants, and then dried at 70 °C overnight.

152 2.3 Characterizations:

153 Synchrotron X-ray diffraction (SXR) was used to study the crystallographic phases, particle
154 size, and microstructure in the synthesised powder samples. At Indian synchrotron Indus-2, the
155 synchrotron measurements were performed on an Angle Dispersive X-ray Diffraction beamline
156 (BL-12) with x-ray wavelength of 0.719 Å²⁴. The morphology and the composition were
157 analysed by FESEM and EDX, respectively (Model: JSM-7610F). FESEM images were
158 captured for the Powder samples. Furthermore, The Oxidation states were confirmed by XPS
159 analysis (Model: Thermo Fisher Scientific Escalab Xi⁺). While Electrochemical measurements
160 (CV, GCD, EIS) were conducted using Platinum mesh as counter electrode and Saturated
161 Calomel as reference electrode in the Biologic SAS, SP-150e (3-electrode Workstation) and
162 CR 2032 Coin cell measurement by done by Bio-logic SAS Battery health cycler system at
163 Battery Fabrication Lab, UPES Dehradun.

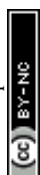
164 3. Results and discussions:

165 3.1 X-ray Diffraction Pattern:

166 Figure 1 presents the XRD patterns of Ni-Co hydroxide (NCH) samples synthesised at varying
167 pH levels. Both Ni(OH)₂ and Co(OH)₂ exhibit two hexagonal polymorphs, α and β , differing
168 in their layer stacking and interlayer composition. As in the α -phase, a hydroxyl-deficient phase
169 having absence of OH⁻ anions but presence of interlayer anions (NO₃⁻), the layers can be
170 stacked randomly along the c-axis with water or anionic intercalates residing within the Van
171 der Waals gap. On the other hand, they can be well-ordered and closely packed along the c-
172 axis, as in the β -phase, which has a stoichiometric composition and an interlayer separation of
173 4.6 Å. The α -phase can form when ammonia is used as the precipitation agent. This is because



174 it can insert anions (NO_3^-) and small molecules (NH_3 , H_2O) into the structure between the
175 layers. After the hydrothermal process, the stoichiometric β -phase is the more stable form
176 because of the process of dissolving and recrystallising²⁵ and its compact brucite-like structure,
177 higher crystallinity, and minimized surface energy under prolonged alkaline hydrothermal
178 conditions. This process enhances phase purity and structural integrity, yielding β -NiCo(OH)₄
179 with superior cycling stability and conductivity. The diffraction patterns of the four samples
180 show peaks at 2θ , = 8.98°, 15.23°, 17.74°, 23.67°, 26.55°, and 28.07°, with d-spacings of 4.63,
181 2.74, 2.35, 1.77, 1.58, and 1.5 Å, respectively. These are the (001), (100), (002), (021), (003),
182 and (111) planes, in that order, of hexagonal structure can be precisely linked to the β phase
183 ^{26,27} (JCPDS 1074-1057). The lattice parameters estimated are $a = b = 3.1639 \text{ \AA}$; $c = 4.6343 \text{ \AA}$;
184 $\alpha = \beta = 90^\circ$; $\gamma = 120^\circ$ are in good agreement with the literature. Also, the peaks for $\pm(001)$,
185 $\pm(002)$, $\pm(110)$, and $\pm(101)$ can be seen at about 5.30°, 10.72°, 16.12°, and 29.24°, with d-
186 spacings of 7.85, 3.88, 2.59, and 1.44 Å. α -phase is also represented by the same space group
187 as that of the β -phase, but with a larger c parameter. The lattice parameters for this phase are a
188 = b = 3.1682 Å; c = 7.8469 Å, which are in good agreement with the literature²⁸. As seen
189 from Figure 1, all four samples contain a mixture of the two phases. Since the space group of
190 both phases is the same, we estimate the molar concentration of the phases by comparing the
191 area under the curve for the same Bragg reflection (reflection (001) in this case). The molar
192 concentration of the α (β) phase in all samples is mentioned in Table S2. The concentrations of
193 α (β) phases were approximately estimated by taking ratio of the area under the highest
194 intensity XRD peaks normalised by $(A/|F_{hkl}|)^2$ in the two phases, where F_{hkl} is the unit cell
195 scattering factor for diffraction by (hkl) planes and A is sum of atomic numbers of all the atoms
196 in the unit cell. The difference in geometric factors like Lorentz polarisation factor and the
197 absorption factor have been neglected in this estimation of phase ratios. We observe that the
198 sample having lower (pH-09) NCH-2, has the lowest concentration of α -phase, followed by the



199 samples NCH-3, NCH-1, and NCH-4. We have estimated the particle size of samples and
200 micro-strain using the Williamson-Hall (W-H) relation ²⁹.

$$201 \quad \beta \cos \Theta = 4. \varepsilon \sin \Theta + K \lambda / d \quad (1)$$

202 In equation (1), β , ε , λ , K , and d are the full width at half maxima (FWHM) of the XRD Bragg
203 peak at diffraction peak 2Θ , micro strain, wavelength of the X-ray, a constant ($K = 0.9$), and
204 particle size, respectively. We have estimated the micro-strain along (00h) by using (001),
205 (002), (003), and (004) diffraction peaks of the β -phase. The W-H plots for the three samples,
206 NCH-1, NCH-2, and NCH-3, are shown in Fig.1(b-d). For sample NCH-4, the W-H plot could
207 not be achieved because of the small peak intensities of the β -phase. The particle size and the
208 micro-strain was calculated from the intercept and the slope of the linear fit, as shown in Figure
209 1(b-d). The particle size and micro-strain are summarised in Table S2. It may be noted that the
210 particle size of the β -phase for the sample NCH-4 and that of the α -phase for all the samples
211 are estimated using the Scherrer formula ³⁰. The α -phase of all the samples shows lower-sized



212 particles (10-16 nm) compared to the β -phase (32-45 nm). Micro-strain of samples NCH-2 and
 213 NCH-3 is found to be much lower (0.06 ± 0.01 %) than NCH-1 (0.145%).

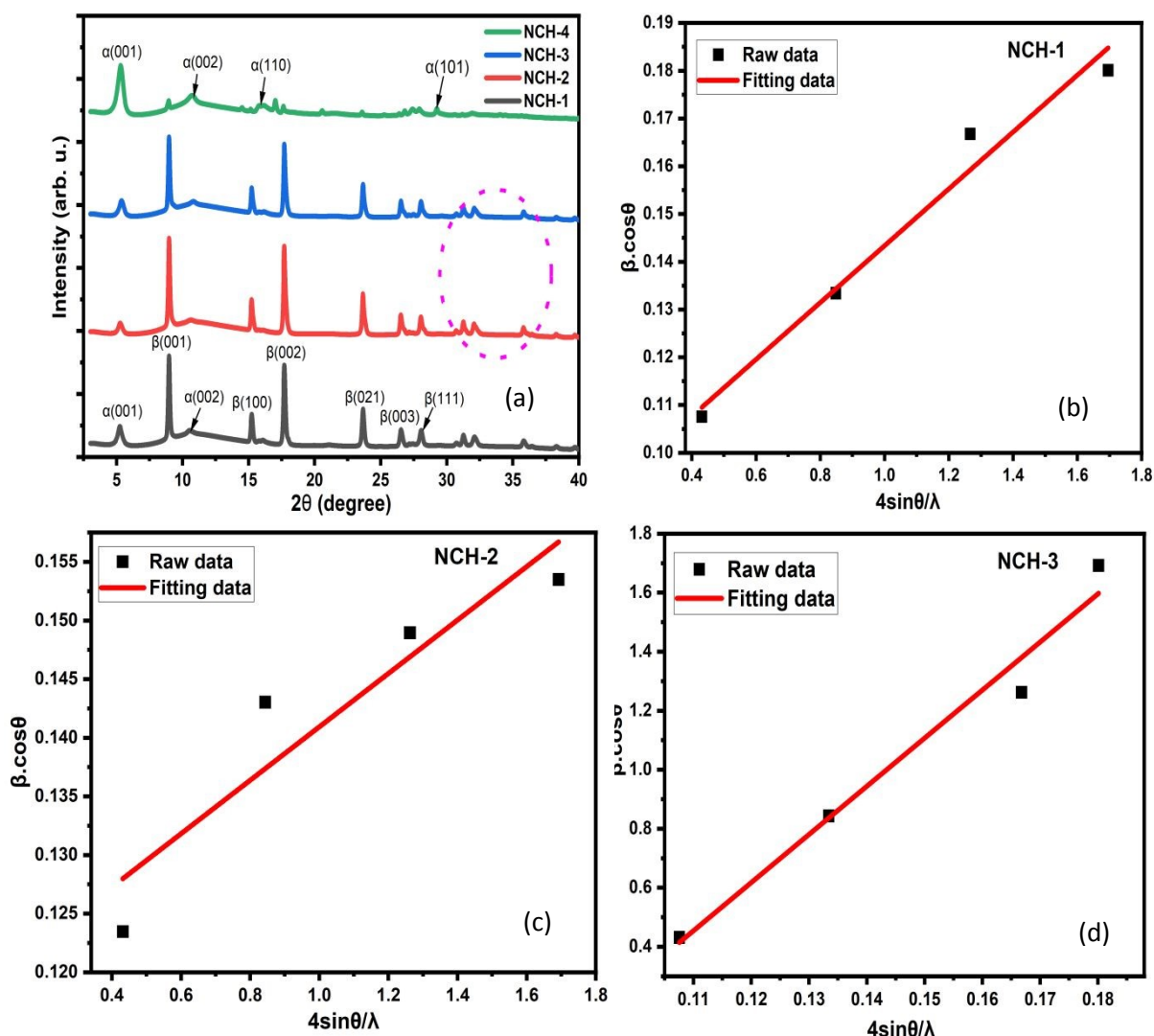
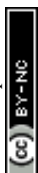


Figure 1: (a) Shows the XRD of NCH samples, while (b-d) presents the W-H plots for NCH-1, NCH-2, and NCH-3 samples.

214

215 3.2 Fourier transform infrared spectroscopy (FTIR):

216 The FTIR spectra of the four samples are shown in Figure S1. The spectra of all the samples
 217 show similar absorption bands. A broad and strong absorption band at 3621 cm^{-1} is related to
 218 O-H stretching modes. A sharper peak for the sample NCH-4 suggested a well-ordered
 219 hydroxyl group in a well-crystallised structure, whereas the sample NCH-1 indicated more



220 hydrogen bonding and interlayer water molecules. The spectra also showed bands at 2414 View Article Online
DOI: 10.1039/D6TA00006A cm⁻¹
221 ¹ and 2847 cm⁻¹, which were related to C-O/C-H group antisymmetric and symmetric stretching
222 modes, respectively. The stretching vibrations of free water molecules in the material are
223 responsible for the peak at roughly 1645 cm⁻¹. Additionally, the N-O band of NO⁻³, which is
224 present in the material's interlayers, is responsible for the peak at 1384 cm⁻¹. In NCH samples,
225 Co/Ni-OH stretching vibrations are represented by the band at 768 cm⁻¹. The stretching
226 vibration of the Ni/Co-O bond is responsible for the peak at roughly 540 cm⁻¹. (NCH 2 and
227 NCH-3 sample shows the sharpest Ni/Co-O bond, suggesting a better crystalline nature).³¹

228 3.3 Morphology and Surface Area Studies

229 3.3.1 Field Emission Scanning Electron Microscopy and EDX:

230 The surface morphology of the four samples in the form of electrodes (active material 80%,
231 carbon black 10%, PVDF 10%) is examined by micro-graphing the surface using FESEM. The
232 high magnification (8 ±1k) with (Scale bar: 1 μm) images are shown in Figures 2(a-d). The
233 overall morphology in all the samples seems to consist of disc-like structures, with a diameter
234 of 1 to 2 μm. However, in samples NCH-1 and NCH-4, the morphology consists of micron-
235 sized discs overlaid on finer particles. In general, the particles in all the samples are big,
236 densely packed, and have slight asymmetry (disc-like). FE-SEM image of Sample NCH-2 at a
237 resolution of 9 K shows more uniform and well-defined discs, and the morphology's apparent
238 openness is a sign of better ion transport channels. At 9 K resolution, the NCH-4 sample shows
239 signs of losing its porosity and having structures that are highly clumped together and not well-
240 defined.



241 Elemental compositions in the four samples were studied using EDX analysis, shown in Figure
242 S2. From EDX analysis, we observe that as the pH of the reactants during sample synthesis
243 increases, the atomic percentage of Ni decreases, and with Co increases, in NCH samples. The
244 variation in Ni/Co ratio is attributed to the pH-dependent precipitation behavior of metal ions,
245 which influences the structural and electrochemical properties of the samples.

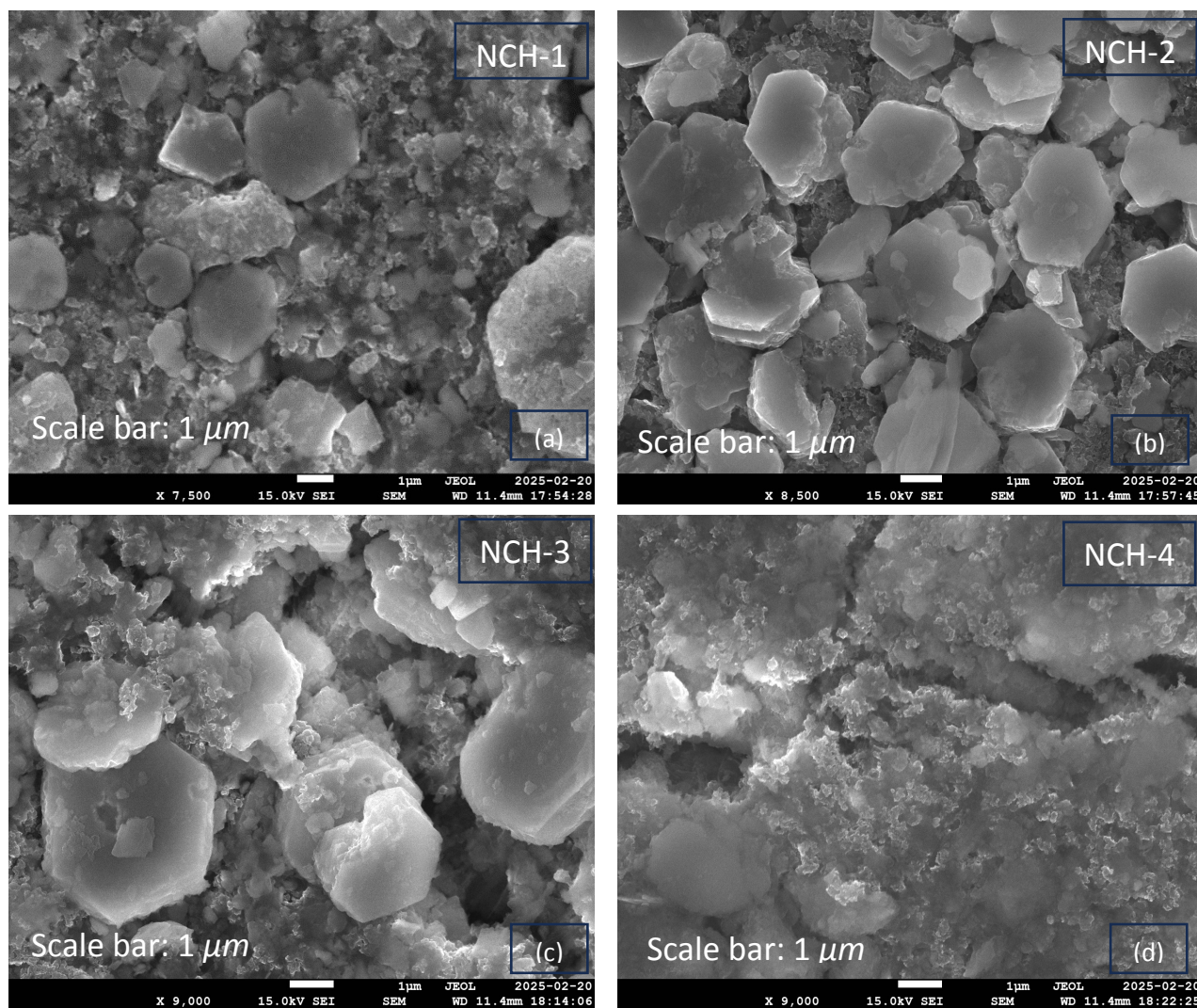
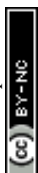


Figure 2: FESEM images of NCH samples showing morphological variations: (a) NCH-1, (b) NCH-2, (c) NCH-3, and (d) NCH-4. Scale bars: 1 μm.

246

247

248



249 3.3.2 Brunauer-Emmett-Teller (BET):

250 BET characterises the specific surface area and the pore size distribution of NCH samples. The
251 Adsorption-desorption isotherms of the samples are shown in Figure S3. All the isotherms with
252 convex shapes and low hysteresis area are of type V, which represents a mesoporous structure
253 with small adsorbate-adsorbate interaction. The pore volume, BET surface area, and BJH
254 surface area were estimated using a literature report by Barrett et al.³² and are summarised in
255 Table S3. Sample NCH-2 shows a minimum BET (BJH) surface area of 12.84 m²/g (13.86
256 m²/g), among the four samples reported in this paper. The same sample also shows the
257 minimum pore volume. This is also corroborated by the FESEM images, where the sample
258 NCH-2 seems most compact and dense. For moderate to high pH values of the reactant during
259 the synthesis of NCH samples, the surface area increases with increasing pH value. The sample
260 NCH-4, synthesised at a pH-11.5 value, showed maximum BET surface area (pore volume) of
261 52.33 m²/g (0.298 cm³/g). Low pH environment inhibits controlled nucleation, promoting rapid
262 crystal growth and aggregation, resulting in dense morphologies with decreased porosity.
263 Because of the limited availability of hydroxide ions restricts precursor hydrolysis and delays
264 nucleation, resulting in non-uniform particle growth and poorly defined structures.

265 In general, it is believed that a larger surface area presents higher storage capacity mainly
266 through intercalation. However, due to various reasons like smaller electrical conductivity in
267 porous systems³³, ionophobic channels, mostly in the case of MOFs and other porous materials
268³⁴, the electrochemical performance of samples is poorer³⁵. Additionally, despite having the
269 lowest BET surface area, NCH-2 exhibits superior performance, indicating that pore structure
270 and ion transport kinetics play a more decisive role than surface area alone.

271

272



273 3.4. X-ray Photoelectron Spectroscopy (XPS):

View Article Online
DOI: 10.1039/D6YA00006A

274 XPS was performed to examine the surface chemical composition and oxidation states of the
275 NCH-1, NCH-2, NCH-3, and NCH-4 samples. The survey spectra confirm the presence of Ni,
276 Co, and O elements in all samples (Figure 3(a) for NCH-2 and Figure S4 for NCH-1,3,4). For
277 the NCH-2 sample, the Ni 2p_{3/2} region (Figure 3b) exhibits distinct peaks at 854.60 eV (Ni²⁺),
278 855.89 eV (Ni³⁺), and a satellite peak at 860.59 eV. The Ni 2p_{1/2} region contains peaks at
279 872.09 eV (Ni²⁺), 873.42 eV (Ni³⁺), and a satellite at 878.66 eV. The presence of Ni³⁺ on the
280 surface suggests the existence of defect states such as Ni vacancies or oxygen interstitials,
281 which are known to improve electrochemical performance by serving as active centres for
282 charge storage^{36–39}. The Co 2p_{3/2} region (Figure 3c) exhibits peaks at 779.53 eV (Co³⁺),
283 781.13 eV (Co²⁺), and 784.68 eV (Co²⁺), while the Co 2p_{1/2} region reveals peaks at 794.67 eV
284 (Co²⁺) and 796.04 eV (Co³⁺)^{40–42}. The O-1s spectrum (Figure 3d) shows two peaks at
285 529.17 eV and 530.12 eV, corresponding to lattice oxygen and metal-oxygen bonding,
286 respectively^{43,44}. For the **NCH-1** sample (Figure S5(a-c)), the Ni 2p_{3/2} peak appears at
287 854.42 eV (Ni²⁺) and the Ni 2p_{1/2} peak at 872.04 eV (Ni²⁺), with no noticeable contributions
288 from Ni³⁺. The Co 2p_{3/2} and 2p_{1/2} peaks are located at 780.40 eV and 796.23 eV, respectively,
289 corresponding to Co²⁺. The O 1s spectrum displays peaks at 529.93 eV (O²⁻) and 531.26 eV
290 (OH⁻ species). In the **NCH-3** sample (Figure S5(d-f)), the Ni 2p_{3/2} spectrum reveals peaks at
291 854.55 eV (Ni³⁺) and 856.74 eV (Ni²⁺), while Ni 2p_{1/2} peaks are seen at 871.92 eV (Ni²⁺) and
292 873.53 eV (Ni³⁺)^{45,46}. The Co 2p_{3/2} region shows peaks at 779.37 eV and 780.86 eV, both
293 associated with Co²⁺, whereas the Co 2p_{1/2} region presents features at 795.06 eV (Co²⁺) and
294 796.51 eV (Co³⁺)⁴⁷. The O-1s spectrum includes peaks at 528.76 eV (lattice oxygen) and
295 529.96 eV (metal-oxygen bonds). Similar to NCH-2, the presence of both Ni³⁺ and Co³⁺
296 indicates the existence of beneficial defect states. For the **NCH-4** sample (Figure S5(g-i)), Ni
297 2p_{3/2} peaks are observed at 854.76 eV (Ni²⁺) and 856.11 eV (Ni³⁺), while Ni 2p_{1/2} peaks appear



298 at 872.36 eV (Ni^{3+}) and 874.11 eV (Ni^{2+}). The Co $2p_{3/2}$ spectrum shows peaks at 779.48 eV and
299 782.84 eV, both corresponding to Co^{3+} , and the Co $2p_{1/2}$ region reveals peaks at 794.60 eV
300 (Co^{3+}) and 796.10 eV (Co^{2+}). The O 1s region shows binding energies at 529.27 eV (metal
301 oxides) and 530.16 eV (M–O–M bonding, where M = Ni or Co). Interestingly, the samples
302 NCH-2 and NCH-3, which contain the majority β -phase composition, exhibit clear Co^{3+} peaks
303 in their XPS spectra. These samples also display enhanced electrochemical performance
304 compared to NCH-1 and NCH-4, which either lack Co^{3+} peaks or exhibit them in lower
305 intensities. This correlation suggests that the presence of Co^{3+} , indicative of Co vacancies or
306 oxygen interstitials, acts as an effective functional site for charge storage, contributing to the
307 improved electrochemical characteristics observed in NCH-2 and NCH-3.

308



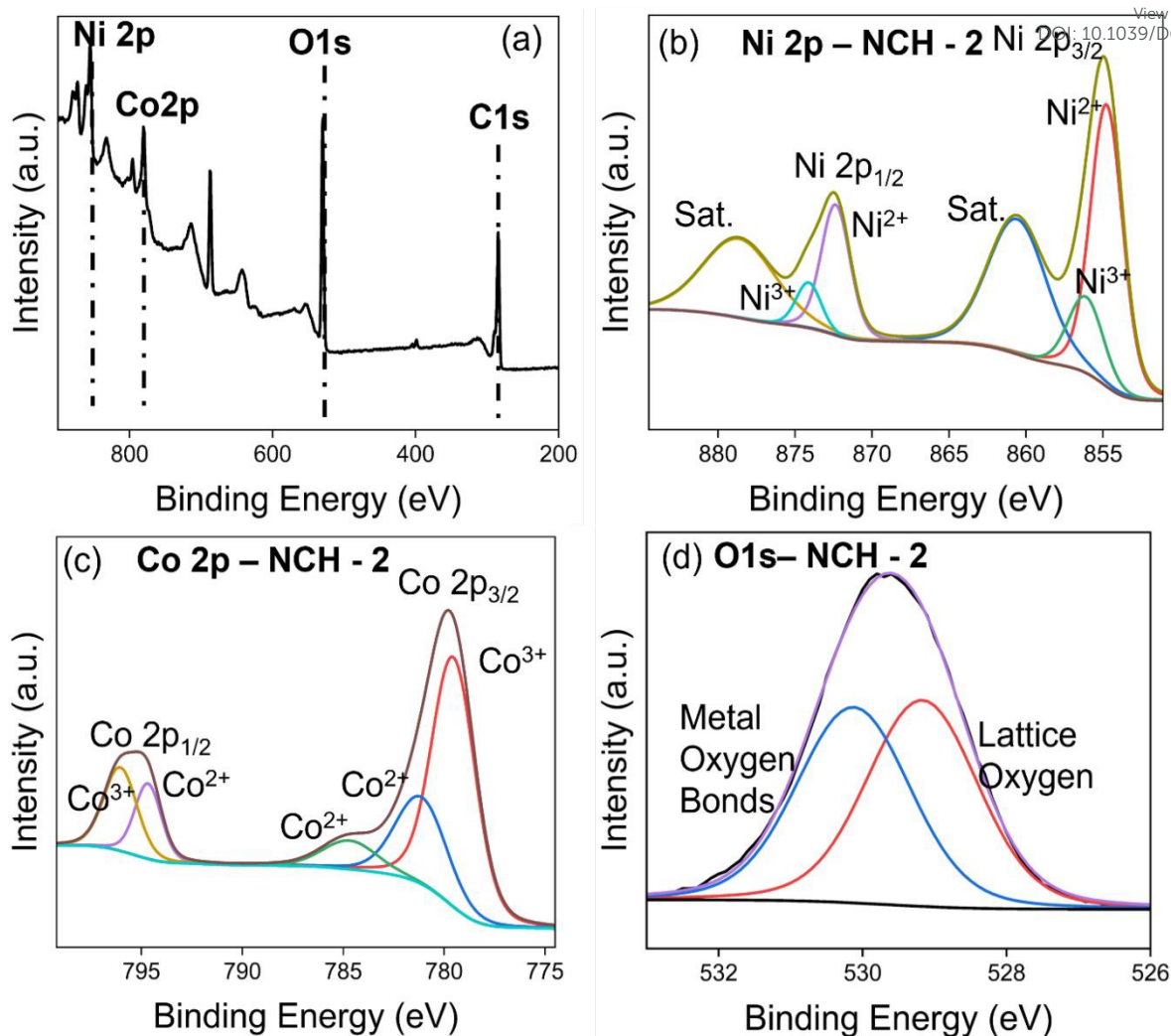


Figure 3: XPS spectrum of NCH-2, (a) Survey scan, (b-d) Ni-2p, Co-2p, and O-1s edges, respectively.

309 3.5. Electrochemical Results:

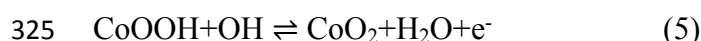
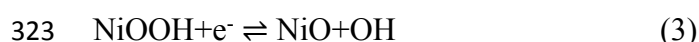
310 The electrochemical studies of NCH-1, NCH-2, NCH-3, and NCH-4 electrodes having mass
 311 loadings of ~ 3.7 , 3.5 , 3.8 , and 3.9 mg cm^{-2} , respectively, on a 1 cm^2 Ni foam substrate were
 312 systematically evaluated in aqueous 3 M KOH electrolyte by using 3- electrode
 313 electrochemical workstation.

314 3.5.1. Cyclic Voltammetry (CV):

315 Figure 4(a) shows anodic and cathodic current as a function of applied potential at 10 mV s^{-1}
 316 scan rate. For the Full CV graph from 1 to 100 mV s^{-1} was see Figure S6. The curves are used



317 to initially assess the electrochemical performances of the electrodes in a 3-electrode
 318 configuration. A pair of redox peaks can be seen in their CV curves for low scan rates in the
 319 anodic peaks as well as for all the scan rates for cathodic peaks, which stem from the reversible
 320 reactions between $\text{Ni}^{2+}/\text{Ni}^{3+}$ and $\text{Co}^{2+}/\text{Co}^{3+}$, which are illustrated in Eqs. (1)-(4) in the
 321 electrochemical redox processes ^{48,49}.



326 The power-law given in Eq. (6) was used to study the charge storage mechanism in the
 327 electrodes. In Figure 4(b), we plot the $\log(I_p)$ versus $\log(v)$ (see Eq. (7)) ^{50,51}.

$$328 \quad I_p = a.v^b \quad (6)$$

$$329 \quad \text{Log}(I_p) = \text{Log}(a) + b.\text{Log}(v) \quad (7)$$

$$330 \quad i_p = b_1 v^{0.5} + b_2 v \quad (8)$$

$$331 \quad \text{DIP}(\%) = \frac{b_1}{b_1 + b_2} \times 100 \quad (9)$$

$$332 \quad \text{SIP}(\%) = \frac{b_2}{b_1 + b_2} \times 100 \quad (10)$$

333

334 Eq. (8) can be rearranged as:

$$335 \quad \frac{i_p}{v^{0.5}} = b_1 + b_2.v^{0.5} \quad (8^*)$$

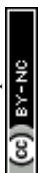
336 A plot of $(i_p/v^{0.5})$ versus $(v^{0.5})$ yields a straight line, where (b_1) and (b_2) are obtained from the
 337 intercept, and slope respectively.



338 And constants a and b are parameters; the value of parameter b depends on the charge storage
339 mechanism. The value of b is close to a value of 0.5 for charge storage by the Diffusion-
340 controlled intercalation process (DIP), whereas for surface-controlled capacitive processes
341 (SCP) of charge storage, the value of b is close to 1⁵⁰. Dunn's analysis reveals that charge
342 storage arises from both capacitive and diffusion-controlled processes, as indicated by b -values
343 of 0.48-0.64 was shown in Table S4 and Figure (4 b). Relative percentage contributions of DIP
344 and SCP were quantified using the equation (8-10) and The NCH-2 and NCH-3 samples show
345 a balanced contribution from both mechanisms, enabling efficient ion transport and improved
346 electrochemical performance. In contrast, the higher diffusion contribution in NCH-4 may limit
347 its rate capability. The specific capacitance as a function of scan rate was calculated using the
348 integrated area under the CV curve and using equation 11 given below¹⁶

349
$$Cs(F.g^{-1}) = \frac{\int IdV}{2 \times v \times m \times \Delta V} \quad (11)$$

350 The specific capacitance as a function of the scan rate is plotted in Figure 4(c). This illustrates
351 the connection between specific capacitance and scan rates (which range from 1 to 100 mV s⁻¹
352 ¹). It was found that at slower scan rates, there is more time for electrolyte ions to reach and
353 interact with the electrode surface, resulting in a higher specific capacitance for the
354 supercapacitor⁵². The capacitance did, however, decrease somewhat when the scan rate
355 increased from 50 to 100 mV s⁻¹. This finding suggests that faster scan speeds restrict ions to
356 the electrode surface, giving them less time to diffuse into the electrode's pores, and the trend
357 is in agreement with the literature⁵³. Out of the four samples, the NCH-2 sample shows much
358 better specific capacitance. Typically, a specific capacitance at a scan rate of 5 mV s⁻¹ was 1230
359 F g⁻¹ observed for the sample NCH-2 compared to 386 F g⁻¹ for the sample NCH-1 and 380 F
360 g⁻¹ for the sample NCH-4. Sample NCH-3 shows moderate specific capacitance of ~ 880 F g⁻¹
361 ¹.



362 3.5.2. Galvanostatic Charge and Discharge (GCD):

363 The GCD plot of NCH samples at 10 A g⁻¹ was shown in Figure 4(d). The electrochemical
 364 performance of all the samples at various current densities was further evaluated, as shown in
 365 Figure S7. The non-linear charging and discharging behaviour of these plots confirms that all
 366 four samples possess characteristics similar to those of battery-like behaviour^{54,55}. The specific
 367 capacitance of electrodes was calculated using Equation (12), and the values are listed in Table
 368 S5. Specifically, the samples NCH-2 and NCH-3 show better storage capacity than samples
 369 NCH-1 and NCH-4, in agreement with the CV results. As the current density increases, the
 370 number of active sites that can be reached decreases because ions have less time to move into
 371 the porous structure of the electrode materials. NCH-2 has the best electrochemical
 372 performance among all the samples. It has the highest specific capacitance of 621 F g⁻¹ at a
 373 current density of 0.5 A g⁻¹, compared to 343 F g⁻¹ at a discharge rate of 0.5 A g⁻¹ for the sample
 374 NCH-4. We find a decrease in capacity as the discharge current density increases, in agreement
 375 with the literature⁵⁶. The rate capability of the samples was evaluated by comparing
 376 capacitance retention at higher current densities. The NCH-1, NCH-2, NCH-3, and NCH-4
 377 samples retain approximately 42%, 75%, 65%, and 26% of their initial capacitance at 5 A g⁻¹,
 378 respectively. Among these, NCH-2 and NCH-3 demonstrate superior electrochemical
 379 performance, exhibiting both higher specific capacitance and better rate capability.

$$380 \quad C_s(F.g^{-1}) = \frac{I \times \Delta t}{m \times \Delta V} \quad (12)$$

381 where I- applied current (mA), Δt - Discharge time, and ΔV - Potential window

382 To decipher the reasons for the superior rate performance of samples NCH-2 compared to the
 383 other samples, because supercapacitor electrodes with low specific surface area (SSA) typically
 384 outperform high-SSA versions in rate capability thanks to their well-designed mesopores,
 385 which promote swift ion movement and cut down on internal resistance, sidestepping the ion



386 entrapment and extended pathways typical of the winding micropores in high-SSA materials.
 387 Consequently, they achieve stronger capacitance retention under high current loads, since
 388 overly high SSA elevates polarization and series resistance amid rapid cycling. Additionally,
 389 we have studied the surface morphology to comment on the reach of the electrolyte to the
 390 electrode active material. We further analyse the XRD data to find out the particle size, micro-
 391 strain, and the fraction of the two stable phases (α and β), to see if the electrochemical
 392 performance has any correlation to these parameters. We have also studied the transition metal
 393 charge states and possible surface defect states using XPS measurements. It may be mentioned
 394 that the structural disordered/defect sites have been related to the centres promoting redox
 395 reactions⁵⁶.

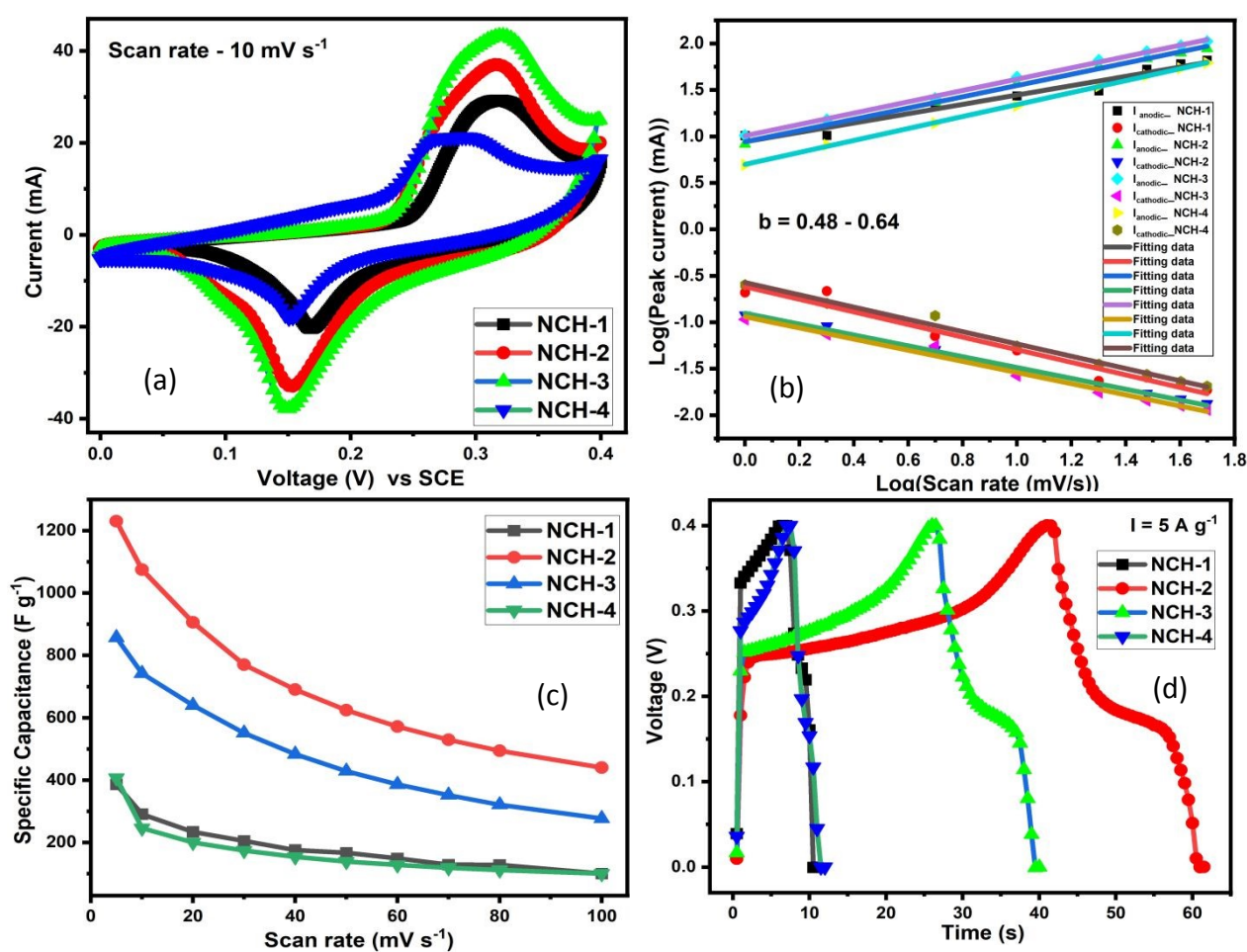


Figure 4: (a-d) Cyclic voltammetry plot of NCH samples at 10 mV s⁻¹. (b) Log-Log plot of Specific capacitance vs Scan rate of NCH samples, (c) Specific capacitance vs Scan rate of NCH samples (d) GCD plot of NCH samples at 10 A g⁻¹.



396 3.5.6. Electrochemical Impedance Spectroscopy (EIS):

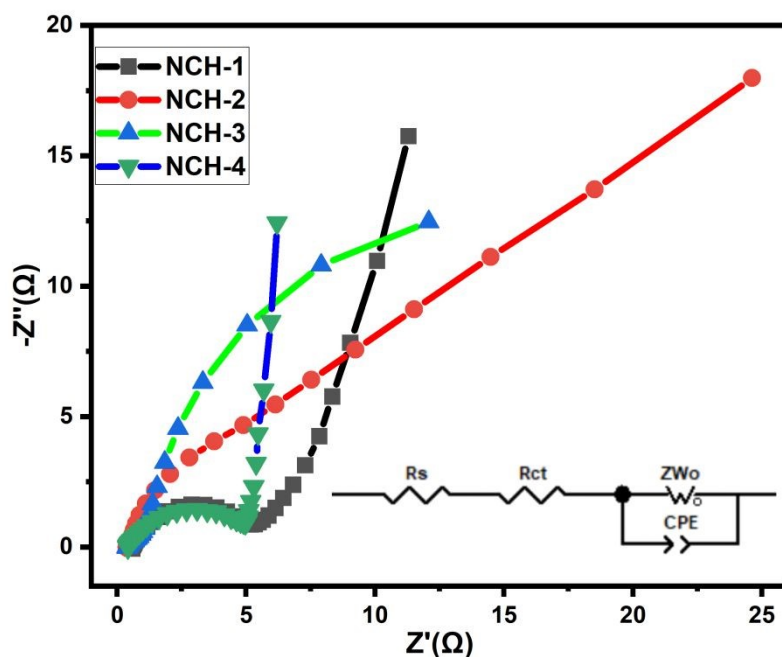
View Article Online
DOI: 10.1039/D6YA00006A

Figure 5: Nyquist plot of NCH samples (Inset: Equivalent Electrical Circuit)

397

398 EIS is extensively used to probe the solution, as well as charge transfer resistance, and to assess
 399 electrode kinetics. Prior to EIS measurements, all electrodes were fully discharged to the lower
 400 potential limit and stabilized to ensure identical electrochemical states. In analysing EIS data
 401 from NCH samples plotted in a Nyquist plot across the frequency range of 100 kHz to 10 Hz
 402 was shown in Figure 5. The impedance spectra were fitted using an equivalent circuit of R_s -
 403 $(R_{ct}\backslash CPE)$ - Z_w . Here, R_s denotes the solution (Electrolyte) resistance, and R_{ct} signifies charge
 404 transfer (polarisation) resistance, which arises from the polarisation of the electrode, causing
 405 current flow through the electrochemical reaction occurring at the electrode surface. Z_w
 406 represents the Warburg element, which is the impedance arising from changes in the diffusion
 407 layer and the rate of diffusion in the working electrode. CPE stands for the Constant Phase
 408 Element, representing electric double-layer capacitance that does not exhibit ideal behaviour.
 409 This model was selected based on the characteristic Nyquist plot features, including a
 410 depressed semicircle at high frequency and a diffusion-controlled region at low frequency. The



411 CPE impedance is expressed as ⁵⁷. $Z_{CPE} = 1/T.(j\omega)^p$, where T is the capacitance pre-factor and
412 P is the frequency exponent. P values of 0 and 1 correspond to pure resistance and dielectric
413 capacitance, respectively. A p-value between 0.8 and 1 indicates a non-ideal double-layer
414 capacitance, with non-ideality arising from roughness, inhomogeneity, and mixed charge
415 storage. We fitted EIS data for four NCH samples, summarised in Table S6. We observed that
416 R_s (=0.21 Ω) and R_{ct} (=0.38 Ω) for sample NCH-2 are the lowest among the four samples
417 reported here. R_{ct} (=0.52 Ω) is also low for NCH-3. This correlates well with the
418 electrochemical performance of the samples, where NCH-2 and NCH-3 demonstrate better
419 performance. The Warburg exponent Z_{w-p} (~ 0.5) for NCH-2 indicates ideal semi-infinite
420 diffusion, while $p > 0.5$ for all other samples signifies finite length diffusion and therefore
421 inferior electrochemical performance ⁵⁸. Similarly, a conclusion was derived from the CPE
422 exponent. For sample NCH-1, a low p (=0.41) indicates a poor-quality surface with a minimal
423 form of kinetic reaction. NCH-3 and 4 show $p \sim 0.97$, which is close to ideal capacitance. For
424 sample NCH-2, p (= 0.72) indicates double-layer capacitance behaviour in this frequency
425 region. Thus, we conclude from the EIS analysis that sample NCH-2 exhibits ideal semi-
426 infinite diffusion in the low frequency (Warburg) region and functions as double-layer
427 capacitance in the high frequency region. Furthermore, the low Chi square error value ($\chi^2 \sim$
428 4.2×10^{-4}) confirms the reliability of the fitting. These results are consistent with the superior
429 electrochemical performance observed for the NCH-2 sample.

430 4. Fabrication of Symmetric Coin Cell-2032 device.

431 To evaluate practical applicability, we fabricated a pair of uniform NCH-2 electrodes, each
432 featuring a 1 cm² active surface and a total mass loading of ~ 1.7 mg. To prevent short-
433 circuiting, we employed a cellulose -based separator that had undergone a 24-hr saturation in
434 the same alkaline 3M KOH electrolyte. Finally, the device was assembled by placing the
435 saturated separator between the electrodes and crimped tightly. ⁵⁹

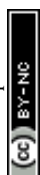


$$436 \quad \text{Energy density (E)} = \frac{0.5 \times C_{\text{sp}} \times \Delta V^2}{3600 \times 1000} \text{ Wh.kg}^{-1} \quad (13)$$

$$437 \quad \text{Power density (P)} = \frac{E \times 3600}{\Delta t} \text{ W.kg}^{-1} \quad (14)$$

438 Where, C_{sp} -specific capacitance, ΔV - Potential window, Δt - discharge time

439 Cyclic voltammetry (CV) measurements were performed between 5 and 100 mV s^{-1} , displayed
 440 quasi-rectangular profiles with noticeable redox features, confirming the coexistence of electric
 441 double-layer and faradaic charge storage was shown in Figure S 8(a). From Figure S 8 (b,c),
 442 The steady rise in current response with increasing scan rate indicates favorable rate
 443 performance. The extracted b-values ($\sim 0.54 - 0.56$) suggest that charge storage is governed by
 444 a combination of surface-controlled and diffusion-limited processes, which is further supported
 445 by Dunn's analysis showing higher capacitive contribution at elevated scan rates. Galvanostatic
 446 charge-discharge (GCD) curves shown in Figure S 8(d) recorded within a 1.5 V window
 447 exhibited nearly symmetric triangular shapes, reflecting good reversibility. The specific
 448 capacitance (Table S7) decreased from 22.0 to 10.0 F g^{-1} as the current density increased from
 449 0.25 to 1.0 A g^{-1} , mainly due to kinetic limitations. The corresponding energy and power
 450 density was calculated from Equation's (13 and 14) and energy densities ranged from 6.86 to
 451 3.13 Wh kg^{-1} , while the power density increased from 178 to 714 W k g^{-1} , demonstrating the
 452 expected trade-off between energy and power. The device retained $\sim 74\%$ of its initial
 453 capacitance after 500 cycles with a Coulombic efficiency of $\sim 93\%$, indicating stable cycling
 454 behavior. Although the energy density is moderate, the Ragone plot (Figure S9) demonstrates
 455 the practical applicability and stable performance of the symmetric device. Further
 456 optimization of electrode architecture and device configuration is expected to enhance the
 457 energy density.



458 Overall, the results confirm that the NCH-2 system exhibits reliable electrochemical
459 performance with mixed charge storage characteristics suitable for practical applications.

460 5. Conclusions:

461 This study demonstrates the successful synthesis of nano-sized bimetallic NiCo(OH)₄ using a
462 surfactant-free co-precipitation/hydrothermal approach, where pH was used as a key parameter
463 to tune the structural and electrochemical properties. The sample prepared at pH 9 (NCH-2)
464 exhibited the most favourable characteristics, achieving a high specific capacitance and
465 excellent rate performance. Through comprehensive analysis involving FESEM, BET, XRD,
466 FTIR, XPS, and EIS, it was evident that the enhanced performance of NCH-2 is linked to its
467 well-developed morphology, presence of structural defects such as cobalt and oxygen
468 vacancies, and superior charge transport dynamics. These findings highlight how subtle control
469 of synthesis conditions, particularly pH, can lead to significant improvements in electrode
470 material performance for energy storage devices

471 **6. Acknowledgement:** The author, Rajkamal Arya, gratefully acknowledges SRF fellowship
472 support from the [CSIR (Delhi), 22D/23J03561]. The authors express gratitude to CIC (UPES)
473 for providing laboratories and characterisation facilities. IIT Ropar is thanked for its assistance
474 with FESEM and XPS analysis, and RRCAT Indore is acknowledged for providing the
475 Synchrotron XRD facility at Indus-2 (ADXRD beamline -12). Archana Sagdeo (RRCAT,
476 Indore) is gratefully acknowledged for many useful discussions.

477 7. References:

- 478 1 P. Vaghela, V. Pandey, A. Sircar, K. Yadav, N. Bist and R. Kumari, *MRS Energy*
479 *& Sustainability*, 2023, 10, 261–276.
- 480 2 R. Kandpal and R. Singh, *ECS Trans.*, 2022, 107, 8133.
- 481 3 K. Patil, P. Babar, D. M. Lee, V. Karade, E. Jo, S. Korade and J. H. Kim,
482 *Sustainable Energy Fuels*, 2020, 4, 5254–5263.



- 483 4 M. Sarfraz and I. Shakir, *J. Energy Storage*, 2017, 13, 103–122.
- 484 5 S. K. Godlaveeti, A. El-marghany, R. R. Nagireddy, S. Gedi and R. Chintaparty,
485 *Ceram. Int.*, 2025, 51, 20620–20627.
- 486 6 R. Arya, T. Dagar and A. K. Sinha, *Phys. Scr.*, 2025, 100, 35927.
- 487 7 B. Huang, W. Wang, T. Pu, J. Li, J. Zhu, C. Zhao, L. Xie and L. Chen, *J. Colloid*
488 *Interface Sci.*, 2018, 532, 630–640.
- 489 8 I. Irshad, A. Nazir, A. Tahir, A. G. Lone and B. Want, *J. Energy Storage*, 2025,
490 107, 114987.
- 491 9 A. Amin, M. Loewenich, L. Grebener, M. Hammad, S. Heckenbach, M.-A.
492 Kräenbring, A. S. Odungat, A. H. Ladole, T. B. Nguyen, D. Schwabenland, H. K.
493 Salim, H. Wiggers, D. Segets and F. Özcan, *ACS Appl. Energy Mater.*, 2025, 8,
494 2050–2063.
- 495 10 Z. Sun, Z. Li, J. Peng, X. Yan, H. Shang, Y. Jin, Q. Zhao, C. Li, S. Lyu, C. Chen
496 and J.-B. Baek, *Energy Environ. Sci.*, 2025, 18, 5159–5189.
- 497 11 Z. Liu, R. Ma, M. Osada, K. Takada and T. Sasaki, *J. Am. Chem. Soc.*, 2005, 127,
498 13869–13874.
- 499 12 T. Zhao, H. Jiang and J. Ma, *J. Power Sources*, 2011, 196, 860–864.
- 500 13 M. Jana, P. Sivakumar, M. Kota, M. G. Jung and H. S. Park, *J. Power Sources*,
501 2019, 422, 9–17.
- 502 14 J. Yin, G. Zhou, X. Gao, J. Chen, L. Zhang, J. Xu, P. Zhao and F. Gao,
503 *Nanomaterials*, 2019, 9, 1686.
- 504 15 M. S. Akhtar, T. Wejrzanowski, G. Komorowska, B. Adamczyk-Cieślak and E.
505 Choinska, *Electrochim. Acta*, 2024, 508, 145284.
- 506 16 R. Arya, T. Dagar and A. K. Sinha, *Ionics (Kiel)*, 2025, 31, 2577–2591.
- 507 17 X. Yi, V. Celorrio, H. Zhang, N. Robertson and C. Kirk, *J. Mater. Chem. A*
508 *Mater.*, 2023, 11, 22275–22287.
- 509 18 M. Bhatt, K. Gautam, A. Sagdeo and A. K. Sinha, *ChemSusChem*, 2025, 18,
510 e202501348.
- 511 19 X. Wang, S. Wang, L. Ren, W. Wu, M. Zuo, W. Xing, B. Zhang, W. Fan, Z. He,
512 Z. Yu, H. Zhang and W. Xiang, *J. Alloys Compd.*, 2024, 977, 173458.
- 513 20 J. Hu, C. Wang, J. Cong, Y. Lan, G. Chen, C. Dong and H. Guan, *J. Energy*
514 *Storage*, 2025, 139, 118826.
- 515 21 X.-Y. You, P.-Y. Lee, S.-C. Wang, C. Kongvarhodom, M. Saukani, S. Yougbaré,
516 H.-M. Chen, K.-C. Ho, Y.-F. Wu and L.-Y. Lin, *J. Energy Storage*, 2024, 100,
517 113678.
- 518 22 T. Gao, X. Xiao, Z. Dong, X. Lu, L. Mao, J. Wang, Y. Liu, Q. Hu and J. Xu,
519 *Batteries*, 2024, 10, 438.



- 520 23 M. Bhatt, B. Gupta and A. K. Sinha, *Sci. Rep.*, 2025, 15, 2192. View Article Online
DOI: 10.1039/D6YA00006A
- 521 24 A. K. Sinha, A. Sagdeo, P. Gupta, A. Upadhyay, A. Kumar, M. N. Singh, R. K.
522 Gupta, S. R. Kane, A. Verma and S. K. Deb, *J. Phys. Conf. Ser.*, 2013, 425,
523 072017.
- 524 25 Y. Tang, Y. Liu, S. Yu, Y. Zhao, S. Mu and F. Gao, *Electrochim. Acta*, 2014, 123,
525 158–166.
- 526 26 J. Zhang, F. Liu, J. P. Cheng and X. B. Zhang, *ACS Appl. Mater. Interfaces*, 2015,
527 7, 17630–17640.
- 528 27 Y. Zhao, X. Zhang, J. He, L. Zhang, M. Xia and F. Gao, *Electrochim. Acta*, 2015,
529 174, 51–56.
- 530 28 T. Mathew, S. Srividhya, K. Venkatesh, L. Thomas and K. Nagaraju, *Inorg.*
531 *Chem. Commun.*, 2025, 174, 114074.
- 532 29 J. S. Lim and F. K. Yam, *Physica B Condens. Matter*, 2025, 699, 416798.
- 533 30 U. Holzwarth and N. Gibson, *Nat. Nanotechnol.*, 2011, 6, 534.
- 534 31 S. Pasieczna-Patkowska, M. Cichy and J. Flieger, *Molecules*, 2025, 30, 684.
- 535 32 E. P. Barrett, L. G. Joyner and P. P. Halenda, *J. Am. Chem. Soc.*, 1951, 73, 373–
536 380.
- 537 33 S. Guo, Y. Wang, S. Xia, H. Li, S. Zuo and W. Xu, *RSC Adv.*, 2025, 15, 11790–
538 11798.
- 539 34 M. Wang, Y. Hou, L. Yu and X. Hou, *Nano Lett.*, 2020, 20, 6937–6946.
- 540 35 B. Shen, Y. He, W. Li, Z. Wang, L. Yu, Y. Jiang, X. Liu, J. Kang, H. Gao and N.
541 Lin, *Mater. Des.*, 2020, 191, 108645.
- 542 36 Q.-R. Pan, S.-J. Li, K. Tong, C. Xie, L. Peng, N. Li, D.-Y. Wang and H. Su, *J.*
543 *Mater. Sci.*, 2019, 54, 9063–9074.
- 544 37 O. A. Shlyakhtin, A. M. Skundin, S. J. Yoon and Y. J. Oh, *Mater. Lett.*, 2009, 63,
545 109–112.
- 546 38 Z. Li, D. Yuan, S. Zhu, P. Fan, H. Ma, Q. Zhang, A. Wen and J. Zhu, *J. Appl.*
547 *Phys.*, 2019, 125, 175103.
- 548 39 Y. Yuan, D. Chen, Y. Luo, T. Gao, C. Zhang, W. Zhang and Z. Yang, *ACS Appl.*
549 *Mater. Interfaces*, 2024, 16, 60404–60414.
- 550 40 K. Bhunia, K. Serbara Bejigo and S.-J. Kim, *Chemical Engineering Journal*, 2024,
551 484, 149306.
- 552 41 Z. Cai, Y. Guo, C. Yang, Z. Li, S. Sun, M. Yue, X. Wang, M. Zhang, H. Wang, Y.
553 Yao, D. Zheng, A. Farouk, F. A. Ibrahim, Y. Lv, X. Sun and B. Tang, *Inorg.*
554 *Chem. Front.*, 2025, 12, 154–160.



- 555 42 X. Zhang, Z. Yang, X. Cui, W. Liu, B. Zou and W. Liao, *J. Colloid Interface Sci.*, 2022, 621, 1–11. View Article Online
DOI: 10.1039/D6YA00006A
- 556
- 557 43 Y. Zhao, H. Li, P. Wang, S. Dong, Q. Wu, Q. Zhang and H. Zheng, *J. Magn. Mater.*, 2023, 580, 170948.
- 558
- 559 44 X. Wei, Y. Chai, N. Liu, S. Qiao, Y. Fu and S. Chong, *Int. J. Hydrogen Energy*, 2022, 47, 9606–9615.
- 560
- 561 45 Y.-L. T. Ngo, L. Sui, W. Ahn, J. S. Chung and S. H. Hur, *Nanoscale*, 2017, 9, 19318–19327.
- 562
- 563 46 S. Muduli, S. K. Pati, T. K. Pani and S. K. Martha, *J. Energy Storage*, 2023, 66, 107339.
- 564
- 565 47 A. Ramesh, N. S. Gudipati, S. R. K. Vanjari and Ch. Subrahmanyam, *Electrochim. Acta*, 2023, 461, 142692.
- 566
- 567 48 X. Ren, L. Ren, Y. Hu, H. Sun, X. Han, C. Xu and H. Chen, *Colloids Surf. A Physicochem. Eng. Asp.*, 2024, 703, 135395.
- 568
- 569 49 Z. Li, C. Shi, J. Yu and L. Bai, *Appl. Surf. Sci.*, 2024, 669, 160534.
- 570 50 S. Li, J. Qiu, C. Lai, M. Ling, H. Zhao and S. Zhang, *Nano Energy*, 2015, 12, 224–230.
- 571
- 572 51 F. Liu, C. Wu, Y. Dong, C. Zhu and C. Chen, *J. Colloid Interface Sci.*, 2022, 628, 682–690.
- 573
- 574 52 J. Chen, J. Xu, S. Zhou, N. Zhao and C.-P. Wong, *J. Mater. Chem. A*, 2015, 3, 17385–17391.
- 575
- 576 53 Y. X. Zhang, M. Huang, F. Li and Z. Q. Wen, *Int. J. Electrochem. Sci.*, 2013, 8, 8645–8661.
- 577
- 578 54 H. Liu, J. Zhu, Z. Li, Z. Shi, J. Zhu and H. Mei, *Chemical Engineering Journal*, 2021, 403, 126325.
- 579
- 580 55 C. Xu, Y. Chen, Y. Ma, J. Huang, J. Zhao and H. Xu, *Electrochim. Acta*, 2021, 367, 137475.
- 581
- 582 56 G. Guo, Y. Mei, X. Chen, J. Liu and W. Liu, *RSC Adv.*, 2023, 13, 25018–25028.
- 583 57 A. Lasia, *J. Phys. Chem. Lett.*, 2022, 13, 580–589.
- 584 58 C. Raminafshar, V. Dracopoulos, M. R. Mohammadi and P. Lianos, *Electrochim. Acta*, 2018, 276, 261–267.
- 585
- 586 59 R. Kumar, S. Tanwar, S. Kalia, Diksha, R. K. Singh and A. L. Sharma, *Diam. Relat. Mater.*, 2026, 163, 113335.
- 587
- 588



Data Availability Statement:

View Article Online
DOI: 10.1039/D6YA00006A

Data are available upon request from the authors

